Reflective metalens with an enhanced off-axis focusing performance

ZAHRAH ALNAKHLI,[1,*] RONGHUI LIN,[1,2] CHE-HAO LIAO,[3] ABDULRAHMAN EL LABBAN,[1] AND XIAOHANG LI[1]

[1] *King Abdullah University of Science and Technology (KAUST), Advanced Semiconductor Laboratory, Thuwal 23955-6900, Saudi Arabia*

[2] *Institute of Materials Research and Engineering, Agency for Science, Technology and Research (A*STAR), Singapore, Singapore*

[3] *Department of Electronic Engineering, National Yunlin University of Science and Technology, Taiwan*

[*]zahrah.alnakhli@kaust.edu.sa

Abstract: Metalenses are one of the most promising metasurface applications. However, all-dielectric reflective metalenses are rarely studied, especially regarding their off-axis focusing performance. After experimentally studying the material optical properties in this work, we propose reflective metalens based on titanium dioxide (TiO_2) and silicon dioxide (SiO_2), which operate at a visible wavelength of 0.633 μm. Unlike conventional reflective metalenses based on metallic mirrors, the proposed device was designed based on a modified parabolic phase profile and was integrated onto a dielectric distributed Bragg reflector periodic structure to achieve high reflectivity with five dielectric pairs. The focusing efficiency characteristics of the metalens were experimentally studied for beam angles of incidence between 0° and 30°. The results reveal that the focusing efficiency for the modified metalens design remains higher than 54%, which is higher than 50%, making it promising for photonic miniaturization and integration.

1. Introduction

Flat mirrors serve as fundamental components in most optical systems, such as microscopes and spectrometers, and have been widely investigated during the history of optics science. However, the potential applications for such components are limited because of their lack of focus and scatter of incident light, although these properties are required in modern optics applications, such as optical tweezers, which use the high focusing efficiency of the incident laser beam for particle trapping and rotation [1–3]. Thus, spherical metallic-based mirrors are most frequently used because they can accurately focus reflected beams at specific positions with diffraction-limited focal spots, trapping and moving small particles. However, integrating these mirrors into another optical system rapidly increases the system complexity because they are thick and bulky, underscoring the need to integrate additional components [4–6]. Another challenge is the optical aberration of optical fields for off-axis applications, requiring further integration of multifunctional optical devices with a specific optical functionality [7,8]. Fabricating such a bulky optical system is highly expensive due to the cost of system engineering and the heavy mass of the proposed optical circumstances [9].

In recent years, metalenses, flat optics patterned with nanostructures, have been promised for various applications, such as optical vortex, focusing, and reflections, due to their high-level integration and miniaturization [10–12]. Among all applications, focusing on reflected light with minimal losses has attracted substantial interest due to the wide applications in laser-beam shaping, spectroscopy, and imaging [13,14]. Some studies on reflective metalenses based on metallic nanopillars and metallic mirrors have been investigated and tested [13,15–19]. However, these structures suffer from a high intrinsic loss of plasmonic materials that prevent the realization of high efficiency in the visible spectrum and are not stable at higher temperature applications like

lasers [9–14]. Another issue with the metallic reflector is the difficulty in fabrication. Building dielectric layers on top of metallic layers is generally more challenging. Moreover, the subsequent etching process would inevitably disrupt the surface roughness of the metallic layers, which reduces the reflection efficiency. These issues can be overcome using dielectric materials to replace metallic nano-antennae, improving the focusing efficiency of the reflected beam [20,21]. However, most recently proposed reflective metalenses suffer from high mirror losses because the mirror structure absorbs a significant portion of the incident beam, reducing the focusing efficiency [22,23].

Furthermore, conventional reflective metalenses use a parabolic phase profile to reshape the wavefront for the reflected beam [24,25]. Because the parabolic phase profile is approximated from the same model as the spherical lenses with a radius of curvature focus beam at the focal point, the beam rays that propagate farther off-axis throughout metalens nano-antenna experience greater deflections. So they intersect the axis in front of the focal point [26]. Thus, this patterning phase profile prohibits the designs from maintaining high focusing efficiency and sub-diffraction limits performance in off-axis angle applications. In other words, if the incident angle of the light beam is not on the optic axis, metalenses with parabolic phase profiles fail to focus the beam at a single point (also called "suffering from a coma"), which degrades the symmetric shape of the focal spot at a high angle of beam incidence. Conventionally, the problem is cured by further integrating multifunctional optics with specific optical functionality, dramatically increasing the cost and thickness of the overall optical setup [27,28].

In this paper, we propose a new design for a reflective metalens, in which the dielectric metalens is integrated with the dielectric distributed Bragg reflector (DBR) to act as a reflective metalens. The resulting all-dielectric reflector was designed to focus incident electromagnetic waves in the visible spectrum at different incidence angles with less optical aberration for off-axis applications. The metalens demonstrates the ease of integrability and minimizes mirror losses resulting in higher focusing efficiency. We start by simulating and optimizing the reflection properties of the DBR part of the device. Then, the required phase profile for minimizing the spherical lens aberration is derived in detail. After the diffraction-limited characteristics of the focal spot are discussed, the performance of the fabricated normal reflective metalens and spherical aberration-free metalens are compared in terms of focusing efficiency and full width at half maximum (FWHM) characteristics at higher incidence angles.

2. Design principles for a reflective distributed Bragg reflector metalens

Figure 1 represents the schematic of the demonstrated dielectric flat reflective metalens. The building blocks of a metalens are TiO_2 nanopillars on a SiO_2/TiO_2 DBR planer that introduce the required phase profile to focus the incident beam on a spot in the reflection mode.

To realize high reflectivity at normal and oblique angles of beam incidence, we followed the following operating principles of the DBR. First, the reflected beams at a certain wavelength must constructively interfere. Thus, the optical path length between reflections from the layer interfaces must correspond to one-quarter of the incident wavelength, which can be achieved if the thickness of each layer fulfils Eq. (1):

$$n_{TiO_2}t_{TiO_2} = n_{SiO_2}t_{SiO_2} = \frac{\lambda_c}{4},\tag{1}$$

where n is the refractive index of TiO_2 and SiO_2, and λ_c (0.633 μm) is the central wavelength at the DBR reflection band. By fulfilling this equation, the path difference between reflections is maintained at the half-wavelength ($\lambda_c/2$), creating a 180° phase shift. High reflectivity can be achieved by increasing the number of DBR pairs and the difference in the material refractive index [29].
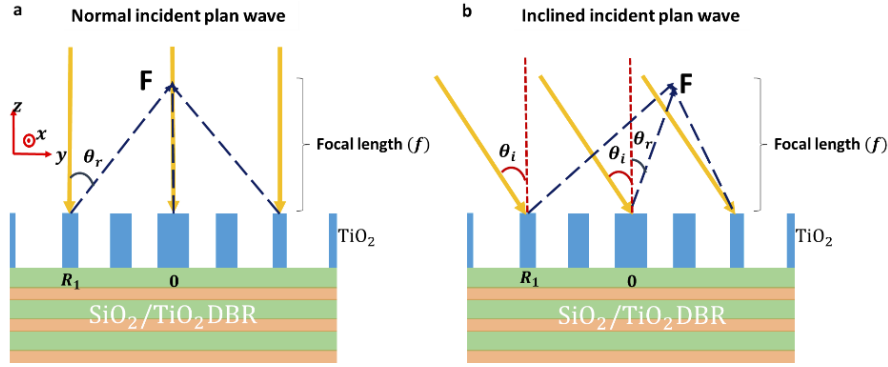
Fig. 1. Schematic diagram of dielectric flat reflector integrated metalens. Nanopillars of TiO_2 on a SiO_2/TiO_2 (DBR) planer create a discrete phase shift and reshape the wavefront of the nonpolarized reflected beam to focus it on the focal point. Schematic of DBR metalens planer focusing: (a) normal and (b) inclined incident light rays.

In common cases, the phase profile of the metalens planer is represented by the following equation [21]:

$$\varphi = \frac{2\pi}{\lambda_c}\left(\sqrt{x^2 + y^2 + f^2} - f\right), \tag{2}$$

where x and y denote the position coordinates of the single nanopillar on the DBR substrate, and f represents the designed metalens focal length. Equation 2 is derived using the infinity point approach, where the incident beam is approximated as a plane wave. This methodology exhibits no coma for normal incidence waves. However, at higher angles ($>10°$), the effect of the spherical lens aberration starts to appear, degrading the shape of the focal spot and expanding its size (see Section IV in the supplementary material). This outcome leads to a reduction in the focusing efficiency of the lens. In conventional spherical lenses, spherical aberration is minimized to almost zero using at least two lenses, and the object is located at a distance equal to the lens radius of the curvature. We applied this approach to correct the metalens coma. Based on the generalized Snell's law [25]:

$$\sin(\theta_r)(n_r) - \sin(\theta_i)(n_i) = \frac{\lambda_c}{2\pi}\frac{d\varphi}{dR}, \tag{3}$$

where θ_i is the incidence angle, θ_r denotes the reflection angle, λ_c represents the designed wavelength, and n_r and n_i denote the refractive indices of reflective and incident media, respectively. As illustrated in Fig. 1, At normal angle of incidence $\theta_i = 0$ and the reflected beam is focused at a point that is normal to the centre of the lens. This result

$$\begin{cases} \sin\theta_i = 0 \\ \sin\theta_r = \sqrt{\dfrac{R_1^2}{R_1^2 + 2f^2}} \end{cases} \tag{4}$$

where $R^2 = x^2 + y^2$,

By Substitution from equations (4) in Eq. (3)

$$d\Phi = \frac{2\pi}{\lambda_o}\frac{R_1}{\sqrt{R_1^2 + 2f^2}}dR$$

To solve for Φ, in order to provide full control of the wavefront, phase shifts covering the range $0 - to - 2\pi$ is needed as well as nanopillar position can take any value from $0 - to-$ lens radius

which could be (R_1). Thus, the modified phase profile becomes

$$\varphi(x_i, y_j) = \frac{4\pi}{\lambda_c} \left(\sqrt{x_i{}^2 + y_j{}^2 + 4f^2} - 2f \right).$$

(5)

Equations (2) and (5) are used to design the metalens with optical parameters of $f = 200$ μm, $d = 300$μm, and a numerical aperture (NA) = 0.6.

3. Experimental method

3.1. SiO$_2$/TiO$_2$ distributed Bragg reflector

Five pairs of SiO$_2$/TiO$_2$ DBRs were deposited on double-sided polished sapphire substrates with thicknesses of t_{TiO_2} = 72 nm and t_{SiO_2} = 110 nm, according to Eq. (1) and Table S1. Then, samples were thermally annealed in ambient air at various annealing temperatures (T_a) with different processing times (t_a).

The simulated reflectance spectrum presented in Fig. 2(a) presents the maximum reflectance of 94% at about 0.633 μm and a stop bandwidth of about 0.235 μm. Figure 2(b) depicts the reflectivity spectrum of the as-deposited sample, followed by thermal annealing for t_a = 30 min at T_a = 40 , 600, and 800 °C. The reflectivity increased from about 86% for the as-deposited sample to 90% for $T_a{>}600$ °C. The central wavelength shifts the designed value as n_{TiO_2} increases as the temperature rises to 800 °C.

In addition, the DBR reflectivity band was gradually modified to approach the theoretical values obtained by the finite-difference time-domain (FDTD) method illustrated in Fig. 2(c). Thus, the SiO$_2$/TiO$_2$ DBR (five pairs annealed at 800 °C) was annealed for different annealing times (t_a = 30, 60, 90, and 180 min). Figure 2(h) displays a significant increase of 5% in reflectivity as the annealing time extended from 30 to 60 min due to the thermal annealing process initiating the crystal structure transformation from Ti$_3$O$_5$ to TiO$_2$ of all TiO$_2$ layers. Then, the reflectivity at λ_c = 0.633 μm decreased to 90% because films started to peel off from the sapphire substrates. Therefore, the five pairs of DBRs annealed at 800 °C for 60 min characteristics were studied further.

Powder x-ray diffraction (XRD) with a Cu kα radiation source was used to study the phase and crystalline structure of TiO$_2$ layers in the DBR structure. Figure 2(d) depicts the XRD pattern of the as-deposited DBR samples annealed at 800°C for 60 min, which were recorded by scanning 2θ between 15° and 40°. The pattern indicates that titanium layers in the as-deposited samples are in form Ti$_3$O$_5$ because the sample has a 2θ peak at 20.6°[30]. In comparison, the annealed sample exhibits different reflectance and transmittance spectra. The 2θ peak intensity at 20.6° is significantly reduced, and a 2θ peak at 25.5° was absorbed, indicating the successful transformation of Ti$_3$O$_5$ to TiO$_2$ due to the thermal annealing process.

Atomic force microscopy (AFM) measurements were performed to evaluate the surface roughness and morphology of DBR samples. Figure 2(e and f) presents three-dimensional (3D) AFM images of the five pairs of SiO$_2$/TiO$_2$ DBRs deposited on sapphire substrates. The measurements were performed on a 5 × 5 μm area. This area was chosen because it is larger than the wavelength of the incident light used for the reflectance measurements. As illustrated in Fig. 2(e), the distribution of grain particles on the as-deposited films is not uniform. However, Fig. 2(f), displaying the annealed sample at 800°C for 60 min, indicates a finer structure with smaller grains. Because TiO$_2$ particles on the DBR surface tend to agglomerate due to the high temperature, the kinetic energy significantly reduces the coalescence of the grains. Furthermore, the root mean square (RMS) in the AFM analysis was used to characterize the surface roughness. The RMS of the as-deposited sample was (3.9 nm), and the surface roughness increased by 1 to 5.1 nm due to the annealing process. The slight increase in the roughness is due to the change in the grain size and film phase.
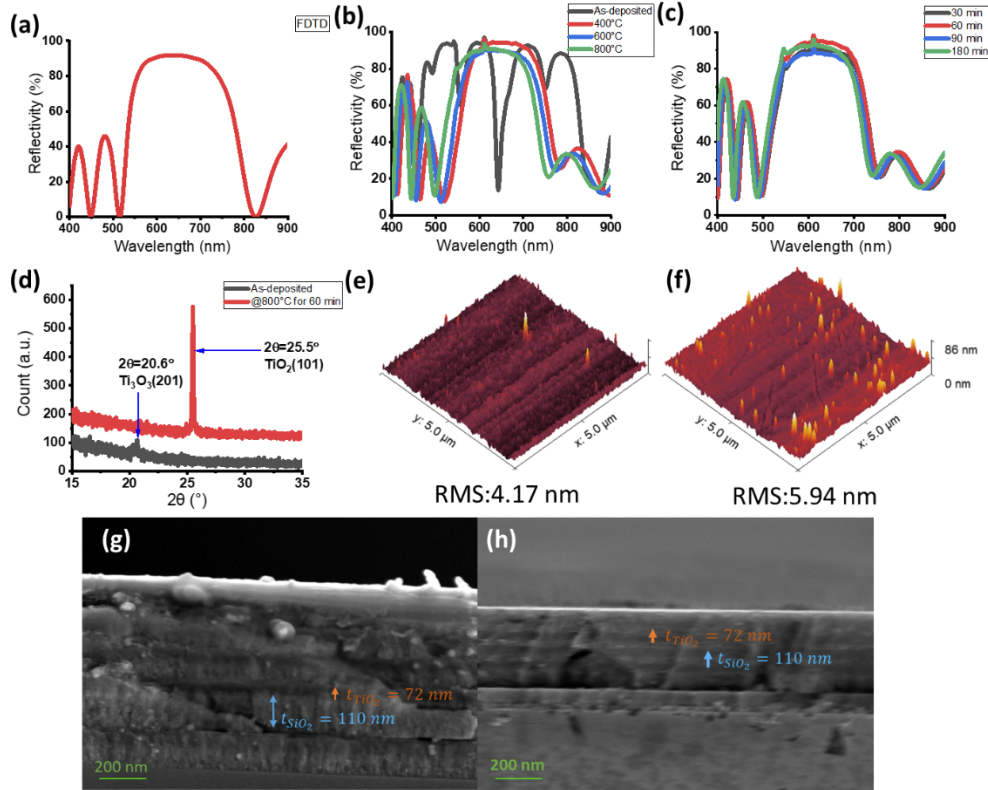
Fig. 2. (a): Simulation reflectivity spectrum for five pairs of TiO_2/SiO_2 (DBRs) using the Lumerical finite-difference time-domain (FDTD) tool. (b) Reflectance vs. wavelength for five pairs of SiO_2/TiO_2 DBRs annealed in ambient air at four annealing temperatures: as-deposited, 400°C, 600°C, and 800°C for 30 min. (c) Reflectance vs. wavelength for five pairs of SiO_2/TiO_2 DBRs annealed in ambient air at four annealing times 30, 60, 90, and 180 min at 800°C. (d) X-ray diffraction (XRD) pattern for five pairs of SiO_2/TiO_2 DBRs deposited on sapphire substrates. The black curve is the XRD pattern of the DBR as-deposited with a peak at $2\theta = 20.6°$, corresponding to the (201) plane of amorphous Ti_3O_5. The red curve is the XRD pattern of the DBR after annealing at 800°C for 60 min, exhibiting a strong peak at $2\theta = 25.5°$, corresponding to the (101) plane of the anatase phase of TiO_2. Atomic force microscopy images and root mean square surface roughness of the top surfaces of five SiO_2/TiO_2 pairs: (e) before annealing and (f) after annealing. Scanning electron microscopy cross-section images for (g) five pairs SiO_2/TiO_2 DBRs as-deposited and (h) after annealing at 800°C for 60 min. Images demonstrate that annealing at high temperatures does not change the film thickness.

According to the design criteria in Eq. (1), depositing DBR layers with precise thickness is critical to obtaining accurate results. Thus, scanning electron microscopy (SEM) cross-section observations of the as-deposited DBR samples annealed at 800°C for 60 min were conducted in Fig. 2(g and h, respectively). Darker regions in both figures correspond to TiO_2 layers, whereas lighter regions indicate SiO_2. The measured spectrum for the layer thickness of both samples was $t_{TiO_2} = 72$ nm and $t_{SiO_2} = 110$ nm. However, the layer interfaces in the annealed samples were more regular and smoother than in the as-deposited samples because of the phase transformation of the titanium oxide layer from the amorphous to the anatase phase.

3.2. Design of a distributed Bragg reflector metalens unit cell

This metalens is a special arrangement of TiO_2 nanopillars at the interface of the TiO_2/SiO_2 DBR, which is designed to reshape the reflected light wavefront by adjusting the location and refractive index of the surface nanopillars. Critically, the choice of nanopillar material depends on its optical properties characterized by the complex refractive index:

$$\tilde{n} = n + ik. \tag{6}$$

For high transmission efficiency, a negligible absorption ($k \approx 0$) and high refractive index ($n>2$) is necessary at the operating wavelength, ensuring high light confinement in propagating media and significantly improving the phase variation from 0 to 2π. Further, the material should be in an amorphous or single-crystalline form because grain boundaries in polycrystalline materials increase light scattering, inducing additional, significant sources of light loss [20]. Thus, we selected crystalline TiO_2 as the nanopillar material because it has zero absorption for the visible wavelength, and its refractive index is $n_{TiO_2} = 2.21$ based on the experimental results discussed in Section II in the supplemental document.

The proposed metalens is a symmetrical 2D planer. Each unit cell with a different effective refractive index (n_{eff}) was positioned at specific x and y positions to realize the conditions given in Eqs. (2) and (5) for conventional and modified metalens, respectively. The subwavelength nanopillars with fixed separation unit cells $P_x = P_y$ and a nanopillar height h realized the total phase profile (Fig. 3(c)). To investigate the nanopillar reflection ability and their full two-phase control, the FDTD method was used to analyze R by fixing $Px = Py$ at 300 nm to meet the Nuquist sampling criterion ($Px = Py<\lambda/2NA$) and changing the nanopillar radius from 40 to 130 nm. Additionally, h was fixed at 600 nm. Figure 3(d) illustrates that a $Px = Py = 300$ nm unit cell can achieve 2π-phase coverage by changing the pillar radius. The arrangement operates at λ between 0.5 and 0.7 µm because TiO_2 nanopillars are placed on the DBR with a bandwidth-operated wavelength. A 2π phase shift can be obtained across the DBR wavelength bandwidth.

To design a nanopillar that implements these properties, we determined a set of periodic nanopillars with a different lattice that provides 2π phase shifts. As depicted in Fig. 3(e), by varying the nanopillar radius as a function of the position (x_i, y_j) on the DBR, the phase shifts of the propagating reflected mode varies from 0 to 2π to match the required phase profile in Eqs. (2) and (5) for conventional and modified DBR metalens, respectively. To build the structure of the metalens on TiO_2/SiO_2 DBRs, we used Eq. (5) for the required phase φ at each position (x_i, y_j) to calculate the required pillar radius.

3.3. Metalens-integrated distributed Bragg reflector fabrication method

This work uses top-down technique to fabricate TiO_2 nanopillars on the DBR. Starting with depositing 600 nm thick TiO_2, the e-beam evaporator process deposited the film on the top surface of the SiO_2/TiO_2 DBR (as deposited) at a substrate temperature of $\leq 400\,°C$. An intense electron beam is emitted from the environment (Angstrom Engineering) filament to strike the source material Ti_3O_5 (CERAC, 99.99%) and vaporize it within a vacuum environment. Then,
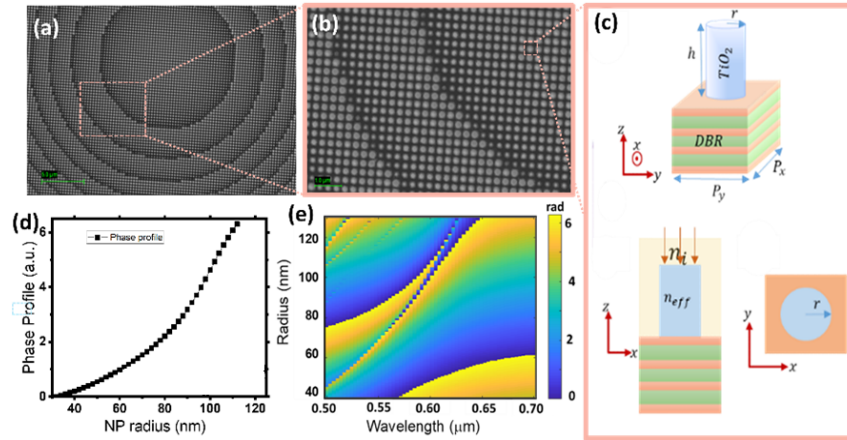
Fig. 3. (a) Top-view scanning electron microscopy (SEM) image of the fabricated metalens on the distributed Bragg reflector (DBR); scale bar: 5 μm. (b) Closer-view SEM image of the DBR metalens; scale bar: 1 μm. (c) Schematic of the building block of the DBR metalens. The top part consists of a TiO_2 nanopillar, with height = 600 nm and radius r on the SiO_2/TiO_2 DBR. The unit cell has a total square cross section with $P_x = P_y = 300$ nm. By changing the nanopillar radius, the phase profile shift of the reflected beam is realized. (d) Computed reflection phase profile shift of the nanopillar as a function of its radius at the wavelength $\lambda = 0.633$ μm. (e) Computed phase map for DBR metalens for wavelengths from 0.50 to 0.70 μm for various sized nanopillars. Each point on the presented map is relative to the phase shift between the radius of the nanopillars and when $n_{eff} = 1$.

the deposited stacks were thermally annealed in ambient air for 30 min at various temperatures, $T_a = 800\,°C$ as previously optimized.

The key to the fabrication of metalens nanopillars is the art of lithography, which was used to create patterns of nanopillars that vary in size with higher resolution. After the wafer was sufficiently cleaned with ethanol and acetone using an ultrasound sonicator, a high-resolution 400-nm-thick positive resist AR-P 6200.09 was spin-coated at 1000 rpm for 60 s. Then, an electron-beam lithography system (Crestec CABL-9000C) at 50 kV was used to transfer the metalens pattern.

Next, to ensure the structural edges were as smooth as possible, a cold development of the photoresists was completed using AR 600-546. A 150-nm-thick Ni layer was deposited by electron-beam evaporation (Angstrom Engineering) as an etching hard mask to ensure high etch selectivity. A lift-off process using AR 600-71 with the aid of O_2 plasma etching was applied to remove residual photoresists.

Subsequently, the reactive ion etch (RIE; Oxford Instrument 5 PlasmaLab System 100 RIE180) with a mixture of $CF_4/O_2/Ar$ gases at a flow rate of 15:5:2 sccm was applied to etch the 600-nm-thick TiO_2 layers. The other conditions of the RIE process were optimized to gain vertical and smooth nanopillar sidewalls. Finally, the rest of the Ni layer was chemically removed using the stripping solution; hence, TiO_2 nanopillars were patterned as the desired size and shape of the designed metalens. The top-view SEM images of a portion of the fabricated DBR metalens with relatively high magnification are displayed in Fig. 3(a and b).

4. Results and discussion

To evaluate the performance of the modified reflected metalens compared to the conventional one, we fabricated two DBR metalenses with two different discretized continuous conversion

phase profiles. The first phase profile given by Eq. (2) was used to fabricate the conventional reflective metalens for $\lambda_d = 0.633\,\mu m$. The second phase profile (Eq. (5)) was used to fabricate the proposed modified DBR metalens. For both designs, the diameter and focal-length values of the micro metalenses were fixed at 300 and 200 μm, respectively. The NA of both metalenses is as large as 0.6. We characterized the 3D intensity distribution of the focused reflected beam by the fabricated metalenses using the custom-built setup in Figure S2(a), whereas the setup in Figure S2(b) was used to characterize the focusing efficiency of the DBR metalenses.

Figure 4(a) presents the experimental focal plane ($x - y$ plane) of the focused beam, as it was reflected by the conventional DBR metalens (phase profile according to Eq. (2)) at the center of the focal plane. The performance of the fabricated lenses was compared with the simulated design obtained using the FDTD method to verify the experimental results. Figure 4(c) of the simulated lens depicts a highly symmetrical focal spot obtained due to the diffraction nature of the reflected laser beam. In optics physics, laser beams are often considered in the form of Gaussian beams. The geometric focus field of a Gaussian beam is determined by the beam wavelength and optical system NA. The designed wavelength of the first DBR metalens is $\lambda_d = 0.633\,\mu m$ and NA = 0.6 at a normal angle of beam incidence. The diffraction limit of the designed device is $D = \frac{\lambda}{2 \times NA} = \frac{0.633}{2 \times 0.6} = 0.527\,\mu m$. The designed focal length as a function of the incident wavelength is 200 μm, but the experimental results demonstrate that the fabricated reflective metalens exhibits a focusing effect within $f = 203\,\text{to}\,205\,\mu m$.
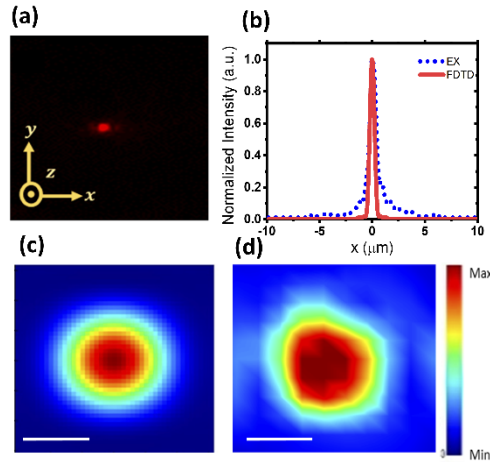

Fig. 4. Experimental and FDTD simulation results for the concave distributed Bragg reflector (DBR) metalens. (a) Diffraction-limited image of the concave DBR metalens focal spot. (b) Normalized intensity profile of the vertical cut of the simulated and experimental concave DBR metalenses at $\lambda_d = 633$ nm with NA = 0.6. (c) Simulated focal spot intensity profile of the designed concave DBR metalens in the *xy* plane at $z = 204$ μm; scale bar: 500 nm. (d) Measured focal spot intensity distribution profile for the fabricated concave DBR metalens; scale bar: 500 nm.

The simulated and experimental results demonstrate that, when the laser beam was normally shone on the top surface of the metalens, the reflected focused light has a Gaussian intensity profile. The vertical cut of the focal spot is also illustrated in Fig. 4(b). The computational measurements indicate a focal spot on the designed metalens with an FWHM of 0.527 μm, whereas the FWHM of the normalized intensity profile of the fabricated lens is measured at 0.608 μm. Although the diffraction-limited FWHM values for both measurements are not equal, the difference between these values (<0.1 μm) is negligible. The focusing efficiency for this

measurement is defined as the ratio of the total power of the beam focused within $3 \times$ FWHM of the normalized intensity profile to the total reflected power by a naked DBR.

Accordingly, the focusing efficiency of the simulated device is about 64%, whereas it is about 62.45% for the fabricated device. The first reason is the imperfect fabrication of nanopillars in relation to the metalens. From Fig. 4(b), nanopillars were designed for a specific wavelength, and NAs have different phase shifts for different pillar radii, leading to different refraction angles of the propagating beam than for what they were designed. In addition, for high aspect-ratio structures with a linewidth of $35 \leq r \leq 120$ nm, height of 600 nm, and spacing of 300 nm, retaining the base diameters as designed is not achievable, leading to tapered sidewall angles for nanopillars, see figure S5. The influence of the tapering angle on the phase profile is minimal since the tapering angle is constant across the whole metalens and a constant phase shift would be expected. The focusing efficiency of the metalens is affected adversely by the tapering angle. However, we are able to get decent focusing performance despite the tapering angle. The effect of the sidewall tapering angle on the metalens phase response and performance is discussed in detail in our previous publication [23]. Second, the resolution limit of the imaging system is used to characterize the proposed metalens. The imaging system is complex and limited by the diffraction limit of all-optical components, such as objective lenses, CMOS cameras, and beam splitters, which have the disadvantage of multiloss sources for beam power while propagating throughout the system.

For the sake of competence, we discussed in Supplemental Document Figure S4, the performance of a device with a similar device, consisting of a gold mirror and TiO_2. As can be absorbed, the performance of this device is better than DBR-metalens one in terms of focusing efficiency above 70% and (FWHM $= 0.517$ μm). These values is less than the theoretical value ($\sim\lambda/2$ N.A. $= 0.527$ μm), which indicates the diffraction-limited focusing of the metallic-metalens. However, while the angle of light beam incidence increased from $0°$ to $30°$, the metallic-metalens shows focusing efficiency above 70% and the transmittance is zero due to high Ohmic loss. This is an unwanted prosperity for several applications like blue and green VCSELs and Resonant Cavity LED applications [31,32].

For the proof of concept demonstrated in Section 3, the intensity profiles of the vertical cuts of the focus beam focal spots as beam angles of incidence increase from $0°$ to $30°$ for the two DBR metalenses, illustrated in Fig. 5(a–h). The vertical cuts are in the xy plane at the measured metalens focal spots located 204 and 198 μm from the metalenses planer (lens focal lengths of conventional and modified DBR metalenses, respectively). Figure 5(a–d) corresponds to the conventional DBR metalens. As displayed in Fig. 5(a), at a normal incidence angle, a highly symmetrical spherical focal spot of the reflected beam is obtained with a corresponding focusing efficiency of $\approx 62\%$. However, at higher incidence angles ($20°$ and $30°$), the conventional DBR metalens displays an obvious expansion of the focus beam focal spot size and a reduction of the planer focusing efficiency to 56.23% and 52.38%, correspondingly. The conventional DBR metalens exhibits the coma effect, where the off-axis beam waves reflected by the lens surface are reflected and focused with more deviation and fail to maintain perfect collimation more than those near the metalens center. This variation reduces the produced image quality and power focused by the optical systems.

Unlike the conventional DBR metalens, the metalens part of the device was constructed by re-engineering the nanopillar distribution according to Eq. (5). Although the focal-length lens was designed at 200 μm, the real focal length was measured at $f = 198$ μm. First, the coma correction characteristics of the modified metalens were demonstrated in Fig. 5(e–h) as the laser-beam incidence angle increases in the same range chosen to characterize the conventional design. A comparison of the corresponding vertical cuts in Fig. 5(a–d) of the focal spot cross sections on the xy plane at $z = 198$ μm with those in Fig. 5(e–h) reveals that the modified DBR metalens provides a larger focal spot (*FWHM* ~ 0.722 μm) and lower focusing efficiency ($\sim 60\%$) when
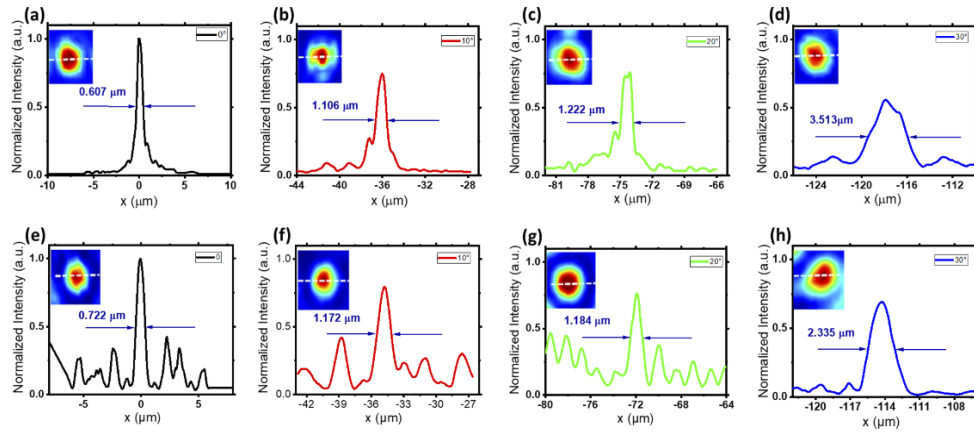
Fig. 5. (a–d) Vertical cuts of the intensity profile of focal spots in the *xy* plane at a different angle of incidence (0°, 10°, 20°, and 30°) for the conventional DBR metalenses. The measured intensity values were normalized to the maximum value recorded for the normal incidence angle. (e–h) Corresponding measurement results for modified DBR metalenses.

the beam is vertically incident to the device surface planer. However, the wavefront aberrations were corrected over higher incidence angles to meet 57.38% and 54.27% for the corresponding angles of 20° and 30°, respectively. Hence, the proposed solution facilitates multipurpose, efficient, integrated optical devices by directly integrating metasurfaces on a highly functional reflective planer, enabling unprecedented light control with random sources. This solution can enable the integration of reflective metasurfaces into optoelectronic device applications in optical communications, tweezers, displays, and other applications. These experimental sites were lower than the maximum achievable computational limit of this design, which can be acquired by further improving the fabrication process, especially by overcoming the proximity effect of electron-beam lithography.

In contrast, both DBR metalens devices were fabricated to operate at the same designed wavelength ($\lambda_d = 0.633$ μm), focal length, lens diameters, and NA. The measured focal length for the modified device is shorter than the conventional design, corresponding to the modified phase profile designed to converge all light rays from different incident angles to the same point, whereas the conventional lens demonstrates obvious divergence. These results provide useful strategies for controlling the focal length. In addition, the results for normal incident light in both cases have a phase profile devoid of spherical aberration resulting in a diffraction-limited spot at a specific design wavelength [33]. However, modified DBR metalenses excel at correcting the problem of coma aberration at higher beam angles of incidence.

5. Conclusion

In conclusion, an all-dielectric reflective metalens with enhanced off-axis focusing performance was designed and fabricated based on the modified parabolic phase profile. The NA for both configurations is 0.6 with a focal length of 200 μm and lens diameter of 300 μm. The experimental measurements demonstrate that both designs could reflect and are capable of diffraction-limited focusing with a recorded efficiency of up to 62% for a normal beam angle of incidence. However, the modified metalens-integrated DBR can also realize higher focusing efficiency of up to 54% at a 30° angle of beam incidence compared with 52% for the conventional design. More interestingly, the small FWHM characteristics of the focused laser beam ($\lambda = 0.633$ μm) explain the higher focusing efficiency for the modified DBR metalens at higher angles of beam incidence.

Finally, the ultrathin design and focusing efficiency are very helpful in developing ultra-compact optics systems and may lead to developments in terms of new conceptual photonic technologies.

Disclosures. The authors declare no conflict of interest.

Data availability. The data presented in this study are available from the corresponding author upon request.

Supplemental document. See Supplement 1 for supporting content.

References

1. T. Li, X. Xu, B. Fu, S. Wang, B. Li, Z., Wang, and S Zhu, "Integrating the optical tweezers and spanner onto an individual single-layer metasurface," Photonics Res. **9**(6), 1062–1068 (2021).
2. J. Liu, C. Wang, W., Wang, and J. Tan, "Mirror based microscope with a super-long working distance in wide spectrum imaging," J. Opt. **15**(7), 075701 (2013).
3. Y.-L. Pan, A. Kalume, I.C.D. Lenton, T.A. Nieminen, A.B. Stilgoe, H. Rubinsztein-Dunlop, L.A. Beresnev, C., Wang, and J.L. Santarpia, "Optical-trapping of particles in air using parabolic reflectors and a hollow laser beam," Opt. Express **27**(23), 33061–33069 (2019).
4. H.-T. Chen, A.J. Taylor, and N. Yu, "A review of metasurfaces: physics and applications," Rep. Prog. Phys. **79**(7), 076401 (2016).
5. S. Chen, Z. Li, W. Liu, H., Cheng, and J. Tian, "From Single-Dimensional to Multidimensional Manipulation of Optical Waves with Metasurfaces," Adv. Mater. **31**(16), 1802458 (2019).
6. S., Liu and T.J. Cui, "Concepts, working principles, and applications of coding and programmable metamaterials," Adv. Opt. Mater. **5**(22), 1700624 (2017).
7. A. Bek, R. Vogelgesang, and K. Kern, "Apertureless scanning near field optical microscope with sub-10 nm resolution," Rev. Sci. Instrum. **77**(4), 043703 (2006).
8. T.A., Klar and S.W. Hell, "Subdiffraction resolution in far-field fluorescence microscopy," Opt. Lett. **24**(14), 954–956 (1999).
9. Y.-Y. Xie, P.-N. Ni, Q.-H. Wang, Q. Kan, G. Briere, P.-P. Chen, Z.-Z. Zhao, A. Delga, H.-R. Ren, H.-D. Chen, C., Xu, and P. Genevet, "Vertical Metasurface integrated Cavity Surface-Emitting Lasers (VMCSELs) for collimated lasing emissions," in *CLEO: QELS_Fundamental Science*. 2019. Optical Society of America.
10. W.T. Chen, A.Y. Zhu, V. Sanjeev, M. Khorasaninejad, Z. Shi, E., Lee, and F. Capasso, "A broadband achromatic metalens for focusing and imaging in the visible," Nat. Nanotechnol. **13**(3), 220–226 (2018).
11. M. Khorasaninejad, W.T. Chen, R.C. Devlin, J. Oh, A.Y., Zhu, and F. Capasso, "Metalenses at visible wavelengths: Diffraction-limited focusing and subwavelength resolution imaging," Science **352**(6290), 1190–1194 (2016).
12. M.L. Tseng, H. Hsiao, C.H. Chu, M.K. Chen, G. Sun, A., Liu, and D.P. Tsai, "Metalenses: Advances and Applications," Adv. Opt. Mater. **6**(18), 1800554 (2018)..
13. H. Yang, G. Li, X. Su, G. Cao, Z. Zhao, X., Chen, and W. Lu, "Reflective metalens with sub-diffraction-limited and multifunctional focusing," Sci. Rep. **7**(1), 1–10 (2017).
14. K. Zhao, H. Zhang, Y., Fu, and S. Zhu, "Specialized directional beaming through a metalens and a typical application," Nanophotonics **7**(1), 339–345 (2018).
15. H. Guo, S. Yue, R. Wang, Y. Hou, M. Li, K., Zhang, and Z. Zhang, "Design of Polarization-Independent Reflective Metalens in the Ultraviolet–Visible Wavelength Region," Nanomaterials **11**(5), 1243 (2021).
16. S. Zhang, M. Kim, F. Aieta, A. She, T. Mansuripur, I. Gabay, M. Khorasaninejad, D. Rousso, X. Wang, M. Troccoli, N., Yu, and F. Capasso, "High efficiency near diffraction-limited mid-infrared flat lenses based on metasurface reflectarrays," Opt. Express **24**(16), 18024 (2016).
17. A. Pors, M. Nielsen, R., Eriksen, and S. Bozhevolnyi, "Broadband Focusing Flat Mirrors Based on Plasmonic Gradient Metasurfaces," Nano Lett. **13**(2), 829–834 (2013).
18. S. Boroviks, R. Deshpande, N., Mortensen, and S. Bozhevolnyi, "Multifunctional Metamirror: Polarization Splitting and Focusing," ACS Photonics **5**(5), 1648–1653 (2018).
19. F. Ding, Y., Chen, and S. Bozhevolnyi, "Gap-surface plasmon metasurfaces for linear-polarization conversion, focusing, and beam splitting," Photonics Res. **8**(5), 707 (2020).
20. R.C. Devlin, M. Khorasaninejad, W.T. Chen, J., Oh, and F. Capasso, "Broadband high-efficiency dielectric metasurfaces for the visible spectrum," Proc. Natl. Acad. Sci. **113**(38), 10473–10478 (2016).
21. M. Khorasaninejad, A.Y. Zhu, C. Roques-Carmes, W.T. Chen, J. Oh, I. Mishra, R.C., Devlin, and F. Capasso, "Polarization-insensitive metalenses at visible wavelengths," Nano Lett. **16**(11), 7229–7234 (2016).
22. F. Aieta, P. Genevet, M.A. Kats, N. Yu, R. Blanchard, Z., Gaburro, and F. Capasso, "Aberration-free ultrathin flat lenses and axicons at telecom wavelengths based on plasmonic metasurfaces," Nano Lett. **12**(9), 4932–4936 (2012).
23. R. Lin, Z. Alnakhli, F., AlQatari, and X. Li, "Analysis of tapered nanopillars for reflective metalens: the role of higher-order modes," IEEE Photonics J. **12**(4), 1–7 (2020).
24. F. Aieta, A. Kabiri, P. Genevet, N. Yu, M.A. Kats, Z., Gaburro, and F. Capasso, "Reflection and refraction of light from metasurfaces with phase discontinuities," J. Nanophotonics **6**(1), 063532 (2012).

25. N. Yu, P. Genevet, M.A. Kats, F. Aieta, J.-P. Tetienne, F., Capasso, and Z. Gaburro, "Light propagation with phase discontinuities: generalized laws of reflection and refraction," Science **334**(6054), 333–337 (2011).

26. M. DelMastro, "Spaceplates: The Final Frontier in Compressing Optical Systems," 2022, Université d'Ottawa/University of Ottawa.

27. H. Mashaal, D. Feuermann, and J.M. Gordon, "Aplanatic lenses revisited: the full landscape," Appl. Opt. **55**(10), 2537–2542 (2016).

28. Y. Sato, A. Miyazaki, K., Mori, and T. Nakamura, "Design of an absolutely aplanatic acoustic lens," Jpn. J. Appl. Phys. **46**(7B), 4982–4989 (2007).

29. B. Gao, J.P. George, J., Beeckman, and K. Neyts, "Design, fabrication and characterization of a distributed Bragg reflector for reducing the étendue of a wavelength converting system," Opt. Express **28**(9), 12837–12846 (2020).

30. N. Rm, K. Gn, S.K. Gundanna, and U.M. Bhatta, "Effect of thermal annealing on structural and electrical properties of tio2 thin films," Thin Solid Films **710**, 138262 (2020)..

31. Y.-Y. Xie, P.-N. Ni, Q.-H. Wang, Q. Kan, G. Briere, P.-P. Chen, Z.-Z. Zhao, A. Delga, H.-R. Ren, H.-D. Chen, C. Xu, and P. Genevet, "Metasurface-integrated vertical cavity surface-emitting lasers for programmable directional lasing emissions," Nat. Nanotechnol. **15**(2), 125–130 (2020).

32. T. Inaba, J. Tatebayashi, K. Shiomi, D. Timmerman, S., Ichikawa, and Y. Fujiwara, "GaN: Eu, O-based resonant-cavity light emitting diodes with conductive AlInN/GaN distributed Bragg reflectors," ACS Appl. Electron. Mater. **2**(3), 732–738 (2020).

33. C. Chen, W. Song, J.-W. Chen, J.-H. Wang, Y.H. Chen, B. Xu, M.-K. Chen, H. Li, B. Fang, J. Chen, H.Y. Kuo, S. Wang, D.P. Tsai, S., Zhu, and T. Li, "Spectral tomographic imaging with aplanatic metalens," Light: Sci. Appl. **8**(1), 1–8 (2019).